

Dilatancy-induced fluid pressure drop during dynamic rupture: Direct experimental evidence and consequences for earthquake dynamics

Nicolas BRANTUT
 Department of Earth Sciences
 University College London
 London, WC1E6BS, UK

Abstract

Dilatancy during rock failure is a key process promoting fluid flow in the crust. Since rock failure is linked to spatio-temporal localisation of deformation, dilatancy is expected to be strongly localised around the fault plane, and to lead to dramatic local reductions in fluid pressure during rupture, potentially impacting dynamic weakening processes such as thermal pressurisation. The existence of coseismic fluid pressure drops have been inferred from field studies, notably in gold deposits which are thought to be formed by this process, but reliable quantitative predictions are still lacking. Here, experimental results are presented where local on- and off-fault fluid pressure variations were measured *in situ* during dynamic rock fracture and frictional slip under upper crustal stress conditions. During the main rupture, the on-fault fluid pressure dropped rapidly to zero, indicating partial vaporisation and/or degassing. Further deformation produced stick-slip events systematically associated with near-instantaneous drops in fluid pressure, providing direct experimental support of the concept of “seismic suction pump”. Extrapolation of the laboratory results indicate that dilatancy-induced fluid pressure drops might be a widespread phenomenon in the crust, counteracting thermal pressurisation as a weakening mechanisms in freshly fractured rock.

1 Introduction

Under upper crustal conditions, the formation of macroscopic shear faults is accompanied with dilatancy, i.e., an increase in porosity due to the growth and coalescence of tensional microcracks (e.g., *Brace et al.*, 1966). Under undrained or partially drained conditions, dilatancy is known to produce significant drops in pore fluid pressure (e.g., *Brace and Martin*, 1968), which has a number of key consequences for fault strength and fluid flow in the crust: a dilatancy-induced

decrease in fluid pressure, through the principle of effective stress, tends to strengthen faults (e.g., *Rice, 1975; Martin, 1980*), stabilise slip (e.g., *Rudnicki and Chen, 1988; Segall and Rice, 1995; Segall et al., 2010*), and may be responsible for episodic hydrothermal circulation in the upper crust (*Zoback and Byerlee, 1975; Sibson et al., 1975; Sibson, 1994*). Geological records of gold deposits in quartz veins indicate that sudden drops in fluid pressure, probably coseismic, trigger the precipitation of minerals and metals (e.g., *Sibson, 1987; Wilkinson and Johnston, 1996; Parry, 1998; Cox, 1999; Weatherley and Henley, 2013; Peterson and Mavrogenes, 2014*). Fault strengthening due to dilatancy at the onset of seismic slip may also counteract fault weakening due to thermal pressurisation of pore fluids, notably by decreasing the initial pore pressure at the initiation of slip, within the rupture process zone (*Rice, 2006; Rempel and Rice, 2006*). Dilatancy can therefore facilitate the occurrence of frictional melting (e.g., *Brantut and Mitchell, 2018*), which has major implications for the dynamics of earthquake slip and energy budget.

While the process of dilatancy is well understood qualitatively, reliable quantitative predictions remain challenging to produce. Dilatancy has been documented experimentally as a bulk phenomenon due to diffuse microcrack opening prior to strain localisation and faulting (*Paterson and Wong, 2005, Chap. 5*). However, the mechanics of faults is also controlled by the dilation occurring within the fault itself. The highly localised nature of rock fracture and fault slip, both in space and time, render the use of averaged, bulk properties (namely, porosity change and material compressibility) inadequate for accurate predictions, which are sensitive to relatively minor variations in poroelastic properties (e.g., *Brantut and Mitchell, 2018*).

Fault zone dilatancy has been measured during slip on synthetic gouge-filled faults (e.g., *Morrow and Byerlee, 1989; Marone et al., 1990; Samuelson et al., 2009*), and significant efforts have been devoted to measure dilatancy/compaction during rapid slip events (e.g., *Ferri et al., 2010; Violay et al., 2015*). While synthetic gouge experiments have been instrumental in the development of our understanding of fault zone dilatancy (e.g., *Segall and Rice, 1995*), they can be challenging to extrapolate to dynamic conditions during earthquakes and to complex fault materials and geometries. In general, volume changes in synthetic gouge are expected to depend significantly on initial consolidation state and the degree of cementation of the gouge. In addition, gouge loss during shear experiments also impacts the accuracy of volumetric measurements for large slip displacements. Finally, gouge experiments are typically performed between planar forcing walls, which masks potential dilatant effects due to natural fault geometry and roughness.

In order to assess quantitatively the role of dilatancy during rock fracture and seismic slip, experimental measurements of fluid volume or fluid pressure change *within* the fault zone at the inception of slip are needed. This paper reports results from a new experimental methodology developed specifically to obtain direct measurements of on- and near-fault fluid pressure during triaxial rock rupture experiments. These new measurements show that near-fault dilatancy produces a dramatic drop of fluid pressure during rupture of intact

crystalline rock, such that the fluid can locally vaporise or degas due to decompression while the fluid pressure a few centimetres away from the fault remains constant. Subsequent stick-slip events on the newly created fault also produce fast drops in fluid pressure. Taken together, these new measurements provide unique constraints on the dilatancy-induced fluid pressure variations occurring during crustal earthquakes in newly formed faults.

2 Methods

The deformation experiments were conducted on thermally-cracked, notched Westerly granite samples equipped with two to four fluid pressure transducers and, in one instance, a set of piezoelectric transducers capable of measuring ultrasonic wave velocities. Cylindrical cores of 40 mm in diameter and 100 mm in length were machined and their faces ground parallel. Two notches of 1.5 mm in width and 17 mm in length were cut at an orientation of 30° from the axis of the cylinders on opposite sides of the sample, in order to favor the propagation of rupture along a predictable plane. The samples were then thermally cracked at 600°C during 5 hours (using a ramp of 4°C per hour), which ensured the formation of a permeable microcrack network (e.g., *Wang et al.*, 2013). The notches were filled with 1.5 mm thick teflon sheets, and the samples were jacketed in a 3 mm thick viton sleeve. Experiments were conducted on two samples. One sample was equipped with 3 pairs of piezoelectric transducers placed in a plane perpendicular to the prospective fault plane, and two differential fluid pressure transducers were placed on the material, one along the prospective fault plane, and one perpendicular to it (see Figure 1, left panel). The other sample was equipped with four differential pressure transducers, three along the prospective fault plane and one across it (Figure S1).

The differential fluid pressure transducers are made of a hollow steel insert facing the sample surface on one side, and closed on the other side by a steel cap sealed by an O-ring (Figure S2). The steel cap is machined on the inside to form a penny-shaped cavity which is connected to the pore space of the rock through the insert, and sealed from the confining medium. The exterior face of the steel cap is equipped with a diaphragm strain gauge sensitive to the elastic distortion of the cap in response to variations of the differential pressure between the confining medium and the pore fluid. The output of the diaphragm strain gauge is amplified with a dynamic bridge amplifier. The fluid pressure transducers were calibrated in situ by changing the uniform pore pressure in the sample while keeping the confining pressure constant (Figure S3). A linear output was observed for all transducers.

Jacketed samples were placed inside the pressure vessel of the UCL triaxial Rock Physics Ensemble (*Eccles et al.*, 2005). Prior to deformation and fracture, the poro-elastic and hydraulic properties of the sample were characterised during a series of hydrostatic loading and unloading cycles (see Figures S4, S5, S6 and S7 for details). The hydraulic properties of the undeformed sample (Figures 1, right panel) show a strong dependence on effective pressure, typical of cracked

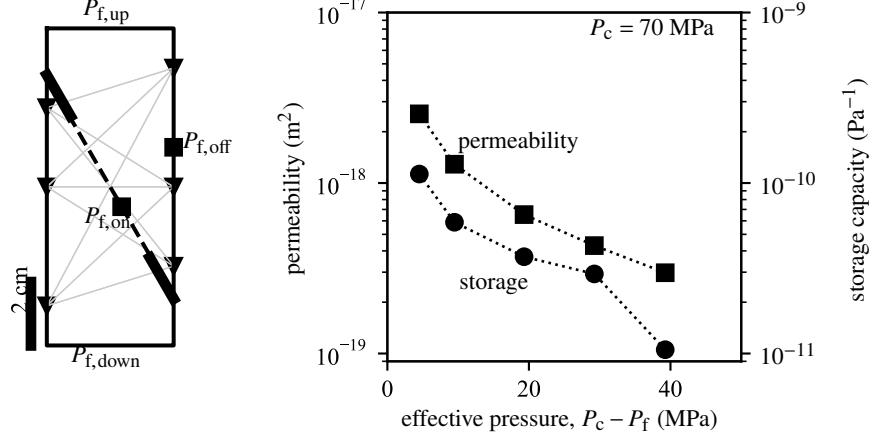


Figure 1: (left) Sample geometry in cross-section, showing the position and length of the 30° notches (thick black lines), the position of fluid pressure transducers (black squares), the position of the piezoelectric transducers (inverted triangles) and the ray paths between them (grey lines). (right) Evolution of permeability (squares) and storage capacity (circles) as a function of the Terzaghi effective pressure under hydrostatic conditions at $P_c = 70$ MPa and step-wise increases in pore pressure.

granite.

The sample equipped with two pore pressure transducers and piezoelectric transducers was tested at a confining pressure $P_c = 70$ MPa and an initially uniform pore pressure $P_f = 30$ MPa. The additional test on the sample equipped with four pore pressure transducers was conducted at $P_c = 60$ MPa and $P_f = 20$ MPa. The deformation tests were performed at a constant axial shortening rate of $10^{-6} s^{-1}$, and a constant pore pressure (20 or 30 MPa) was maintained at both ends of the sample (downstream and upstream). The volume in the pore fluid intensifier was recorded to give access to the finite pore volume change in the samples when pore pressure was equilibrated throughout the pore and tubing network. All mechanical data, including outputs of fluid pressure transducers, were recorded at a nominal rate of 1 Hz, and the sampling rate was increased to 5 Hz during rupture and slip events.

3 Results

3.1 Fluid pressure drop during rupture

During deformation in the test conducted at $P_c = 70$ MPa and $P_f = 30$ MPa, the differential stress initially increased linearly with increasing axial strain (Fig-

ure 2a), and the pore volume initially decreased, reached a minimum and then increased with increasing deformation (Figure 2c). Concomitantly, the pore pressure measured inside the sample remained almost constant (within a few megapascals) up until the peak stress (Figure 2e). In the few minutes prior to macroscopic failure of the sample, the applied stress reached a peak, decreased progressively and underwent a small sudden drop (Figure 2b), accompanied by a small drop in both on- and off-fault pore pressure ($P_{f,on}$ and $P_{f,off}$, respectively) (Figure 2f). With increasing deformation, the applied stress decreased further, accompanied by accelerated deformation and dilatancy. Together with this acceleration, the internal fluid pressure measured on the fault trace $P_{f,on}$ started decreasing rapidly, and suddenly dropped to zero (within the accuracy of the transducer calibration) during the macroscopic failure of the sample (Figure 2f). The pore pressure measured off the fault trace, $P_{f,off}$, followed a similar pattern but after some delay, and its drop was more progressive and toward a small but nonzero value $P_{f,off} \approx 2.3$ MPa. This overall pattern was reproduced in the additional test performed at $P_c = 60$ MPa and $P_f = 20$ MPa (Figure S8).

After rupture, $P_{f,on}$ remained around zero and $P_{f,off}$ remained at 2.3 MPa for around 250 s, while the pore fluid volume (as measured externally from the pore pressure intensifier volume change) kept increasing almost linearly with time. In the final stage, $P_{f,off}$ started increasing, followed by $P_{f,on}$, asymptotically reaching the set pressure $P_{f,up} = P_{f,down} = 30$ MPa. Considering a pore pressure difference of the order of 2 MPa between the off- and on-fault locations, measurement of fluid flow rate into the fault zone during the post-rupture fluid recharge yields an off-fault permeability of around 4×10^{-18} m², which is comparable to the permeability of the undeformed material at near-zero effective pressure (Figure 1).

3.2 Wave speed variations during rupture

The P wave speed of the undeformed sample was initially uniform and isotropic, equal to around 6 km/s. Prior to the main rupture event, the P wave speed measured along the fault trace and along the horizontal (perpendicular to the compression axis) decreased progressively from the intact value down to around 5.5 km s⁻¹ and 5.3 km s⁻¹, respectively (Figure 3, path A and B). By contrast, the P wave speed along a subvertical direction across the fault trace did not show any significant decrease before rupture (Figure 3, path C). While the main rupture event itself was very sudden, the P wave speed measured along the fault and along the horizontal axis (paths A and B) decreased progressively and stabilised while the on-fault fluid pressure remained zero. During the fluid pressure recharge towards $P_{f,on} \rightarrow 30$ MPa, the P wave speed (paths A and B) decreased again progressively. The P wave speed averaged across the fault in a subvertical orientation (path C) exhibited the same features but the amplitude of the change was much lower (only around 100 m s⁻¹ just after rupture) and more gradual, highlighting the highly localised nature of the variations in wave speeds.

In summary, the wave speed measurements show a clear two-step decrease

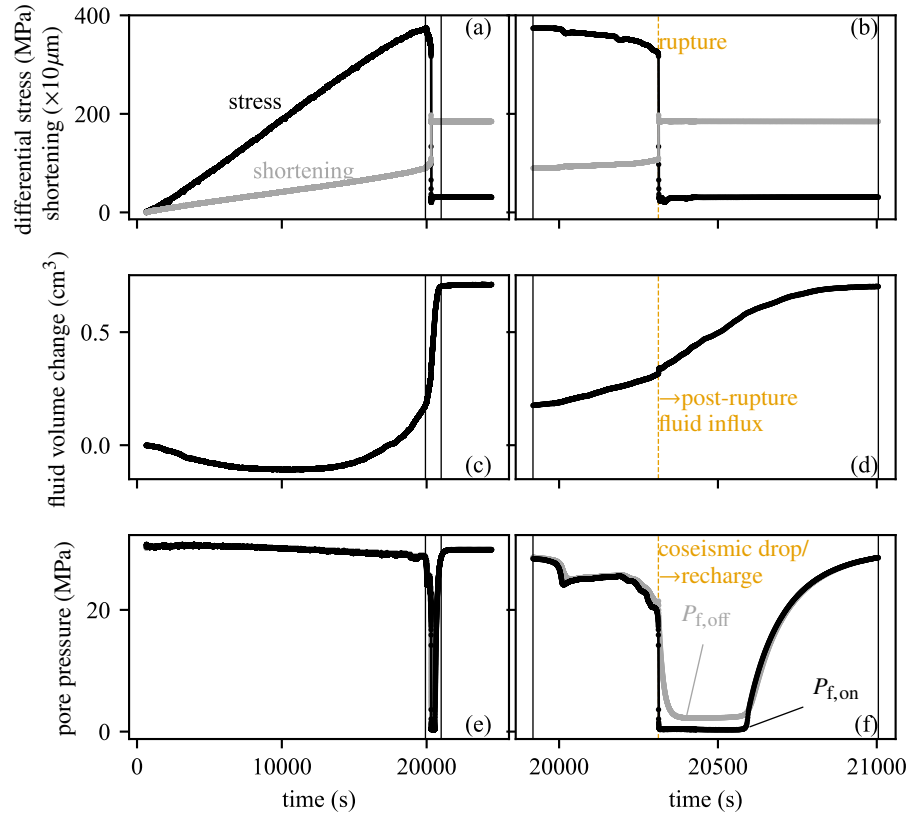


Figure 2: Test conducted at $P_c = 70$ MPa and $P_f = 30$ MPa. Differential stress and axial shortening (a,b), fluid volume change (c,d) and on- and off-fault pore pressure (e,f) as a function of time during the triaxial rupture experiment. Panels (b,d,f) correspond to the time period marked between the thin vertical lines in panels (a,c,e).

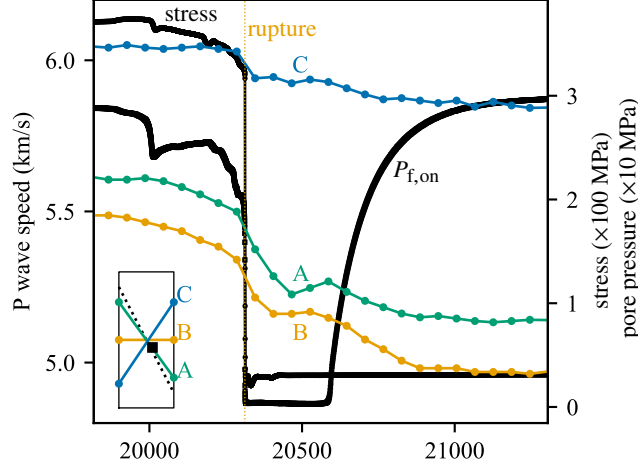


Figure 3: Test conducted at $P_c = 70$ MPa and $P_f = 30$ MPa. Evolution of differential stress, on-fault pore pressure, and P wave speed along (path A, green) and across (paths B, orange, and C, blue) the fault during rupture.

along paths A and B: a first large drop, followed by a plateau and then a smaller gradual decrease. Along path C (diagonal orientation across the fault), only a small, gradual decrease is observed after rupture.

3.3 Fluid pressure drop during subsequent slip events

After the main rupture, further axial shortening resulted in a series of dynamic stick-slip events along the newly-created fault. Prior to stick-slip, the differential stress increased elastically (Figure 4a), which was accompanied by a small increase in on- and off-fault fluid pressure (Figure 4c). Stick-slip was marked by a sudden stress drop and a step in axial shortening, and systematically accompanied by a sudden drop in on-fault fluid pressure, typically of a few megapascals in amplitude (Figure 4c), followed by a slow recovery. Compared to the on-fault fluid pressure, the off-fault fluid pressure decreased more progressively and the net drop was smaller. The fluid pressure recovery occurred at a similar rate for both on- and off-fault locations, and was accompanied by an influx of fluid (as measured by the total pore volume change, Figure 4b). No significant wave velocity change was measured prior to or after stick-slip events.

In addition to stick-slip events, stable slip was also observed. A series of slip steps were conducted at a slip rate of $11.5 \mu\text{m/s}$ for durations ranging from a few seconds to tens of seconds. The on-fault fluid pressure decreased continuously with on-going slip, while the intensifier volume remained constant (i.e., the sample was macroscopically undrained) (Figure 5). The fluid pressure measured off-fault also decreased, but with a significant delay (Figure 5c, blue curve), indicating that the pore volume source was localised on the fault. When slip

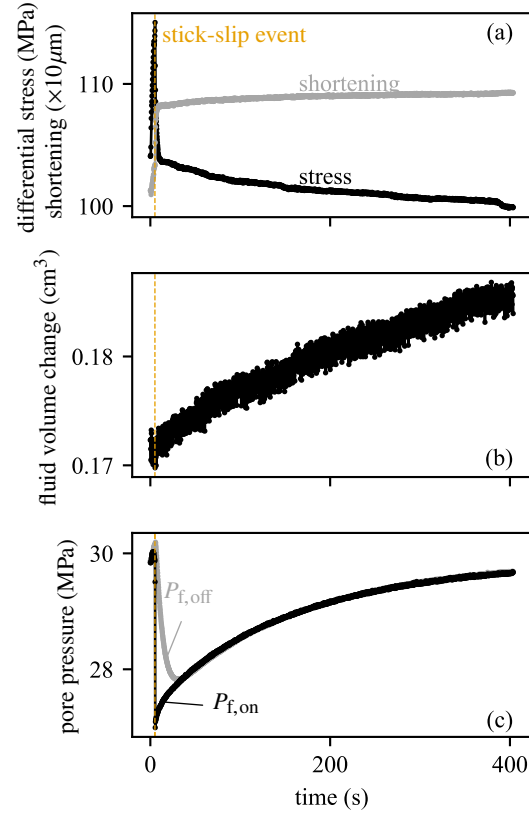


Figure 4: Test conducted at $P_c = 70$ MPa and $P_f = 30$ MPa. Differential stress and axial shortening (a), fluid volume change (b) and on- and off-fault pore pressure (c) as a function of time during a stick-slip event.

was stopped, the pore pressure gradually recovered and the intensifier volume change indicates that a significant pore volume increase occurred.

The observation of a pore pressure drop during slip was systematic for slip rates above $10 \mu\text{m/s}$. After each imposed slip episode, shortening was stopped until complete reequilibration of pore pressure throughout the sample. By recording the net variation in pore fluid intensifier volume after slip and pore pressure reequilibration, an estimate of the sample pore volume change incurred by fault slip is obtained (Figure 6a). For both tests, the pore volume change increased more or less linearly with increasing imposed slip. In the sample fractured at $P_c = 70 \text{ MPa}$ and nominal $P_f = 30 \text{ MPa}$, the maximum recorded pore volume change was of around 0.08 cm^3 after 0.97 mm slip. By contrast, in the sample fractured at $P_c = 60 \text{ MPa}$ and $P_f = 20 \text{ MPa}$, the largest recorded pore volume change was of 0.03 cm^3 at 1.04 mm slip. Using a representative, rather conservative fault width of 3 mm , the observed pore volume change translate to a maximum of $+1.12\%$ and $+0.42\%$ fault zone porosity increase after around 1 mm slip in the sample tested at $P_c = 70$ and $P_c = 60 \text{ MPa}$, respectively. The difference in dilatancy rate per unit slip between the two samples tested indicates some variability in either fault geometry or internal structure that could be attributed to the slightly different pressure conditions tested, but also to the natural variability in fault structures formed in experimentally faulted granite.

The peak pore pressure drop recorded during each slip episode increases approximately linearly with increasing pore volume change, in a trend common to both samples (Figure 6b). The pore pressure drop recorded by on-fault transducers is a lower bound for the actual pore pressure variation inside the fault, due to (1) the nonzero internal volume of the transducers, and (2) nonzero drainage from the pore space within the fault walls, notably during controlled slip episodes at $11.5 \mu\text{m/s}$. Despite those limitations, the overall trend of pore pressure drop as a function of net pore volume change appears quite robust. The variability observed during slip episodes associated with low pore volume change is likely due to the existence of a range of drainage conditions, from near-perfectly undrained events during stick-slip to partially drained events during fast but controlled slip. In all cases, stick-slip events were preceded by some stable, controlled slip, so it was not possible to completely separate the pore volume change associated with each phase. The approximately linear relationship between pore pressure change and pore volume change provides an estimate of the compressibility of the fault zone material, here of the order of $C_{pp} = (1/\phi)\partial\phi/\partial P_f \approx 2 - 4 \times 10^{-8} \text{ Pa}^{-1}$, using a nominal fault porosity ϕ_0 between 2 and 4%.

4 Microstructures

A very clear, single shear fault was formed and slipped in both tested samples. Detailed observations were performed of the fault structure formed during the test conducted at $P_c = 70 \text{ MPa}$ and $P_f = 30 \text{ MPa}$. After vacuum impregnation in epoxy resin, the sample was cut perpendicular to the fault plane and

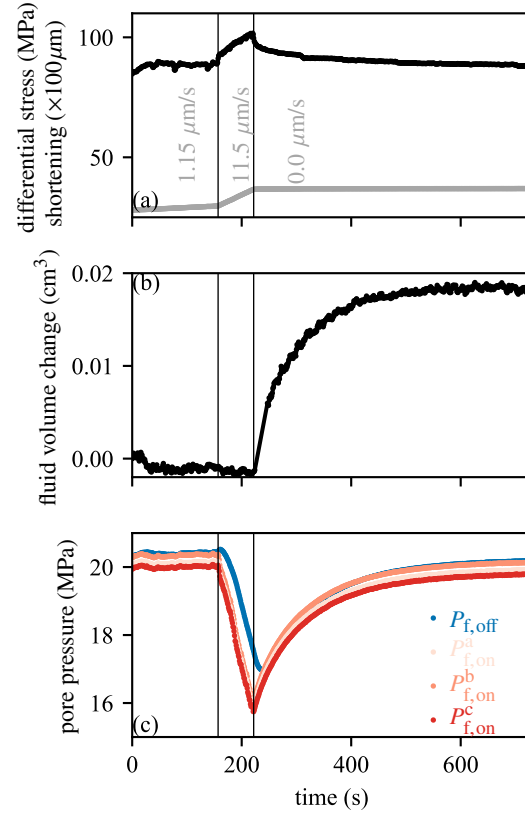


Figure 5: Test conducted at $P_c = 70$ MPa and $P_f = 30$ MPa. See Figure S1 for sample geometry and labelling of pore pressure transducers. Differential stress and axial shortening (a), fluid volume change (b) and on- (red) and off-fault (blue) pore pressure (c) as a function of time during a slip-rate step from 1.15 to 11.5 $\mu\text{m/s}$.

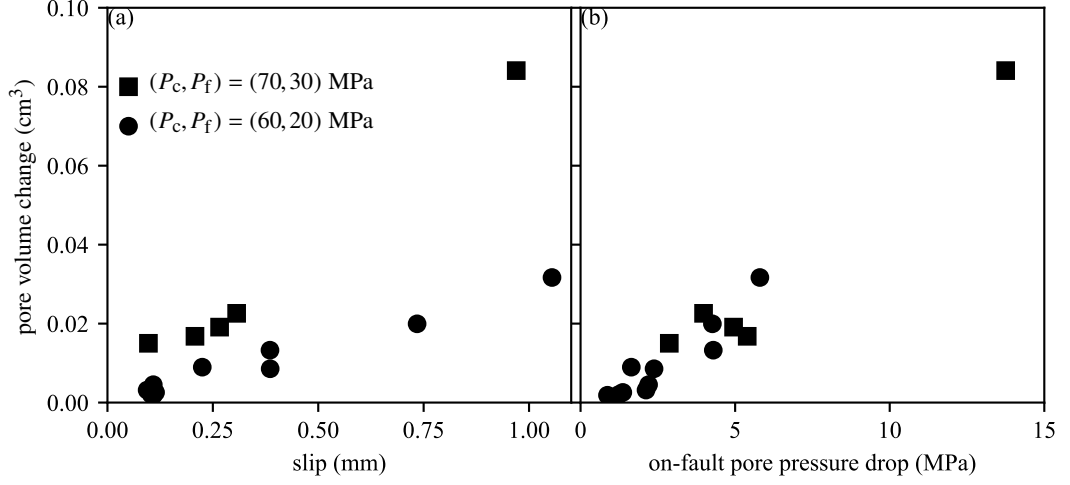


Figure 6: Pore volume change as a function of slip (a) and on-fault peak pore pressure drop (b) during all slip episodes (controlled at $11.5 \mu\text{m/s}$ and stick-slip).

the entire surface was polished down to a $0.5 \mu\text{m}$ grit. At sample scale, the fault zone connects the two notches at the average angle of 30° , but contains more than one strand and appears undulous (Figure 7a). The internal structure of the fault zone, observed with a Scanning Electron Microscope (SEM), consists of a gouge zone delimited by two main boundary faults (Figure 7b). The overall fault zone thickness where intense microfracturing and cataclasis is observed is of around 3 mm. The transition from the gouge zone to fault walls is sharp, and off-fault damage is present in the form of thin intra- and inter-granular tension cracks oriented along the compression direction located within 1 to 2 mm from the gouge boundary (Figure 7c). The internal structure of the gouge zone itself is complex. Multiple cataclastic shear zones oriented at 30° from the compression axis cut heavily microcracked lenticular pieces of the parent rock (Figure 7b). In addition, thin shear zone with intense grain size reduction are present in the central part of the gouge zone, with offsets of several millimetres highlighted by sheared mica grains (Figures 7d,e). The total slip accumulated across the fault was 5.2 mm, which is significantly larger than the largest of the observed offsets across any single thin cataclastic band, which indicates that several bands must have operated either sequentially or collectively to accommodate the total imposed slip.

The thin shear bands consist mostly of dense, finely comminuted material (Figure 8a), sometimes containing at their center some material derived from a sheared mica, with undulating boundaries and flow structures (Figure 8b). In places, the material forming the shear zone transitions from a dense, fine-grained granular aggregate to a completely nonporous continuous matrix containing traces of chemical heterogeneities aligned with the shear plane (Figure

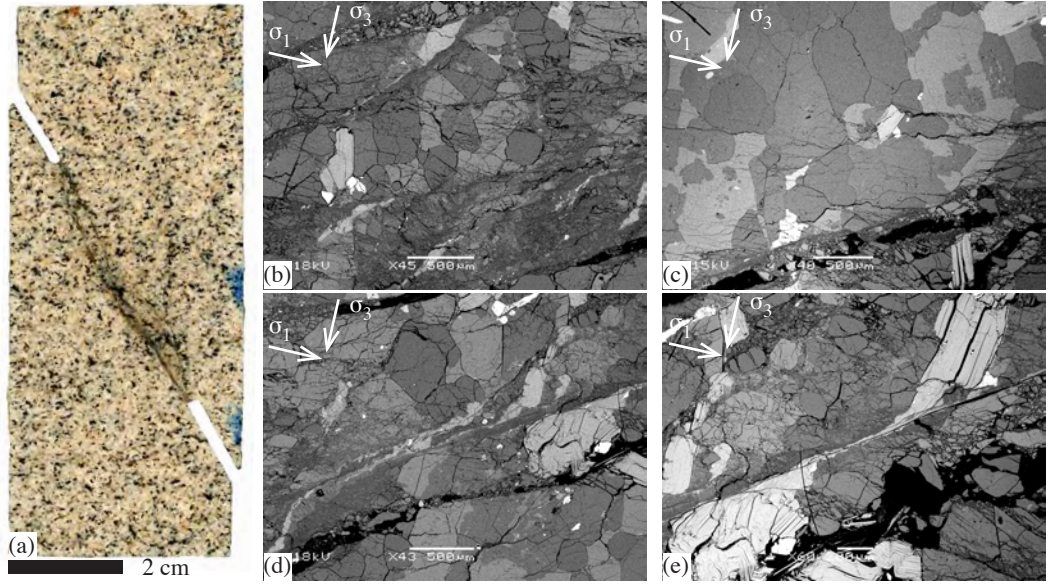


Figure 7: Fault zone structure in the sample tested at $P_c = 70$ MPa and $P_f = 30$ MPa. (a) Optical image of the whole sample after polishing (notches were filled with a Teflon sheet during the test itself). (b-e) SEM Backscattered electron images of the internal structure of the fault; the orientation of remotely applied principal stresses is indicated by the white arrows.

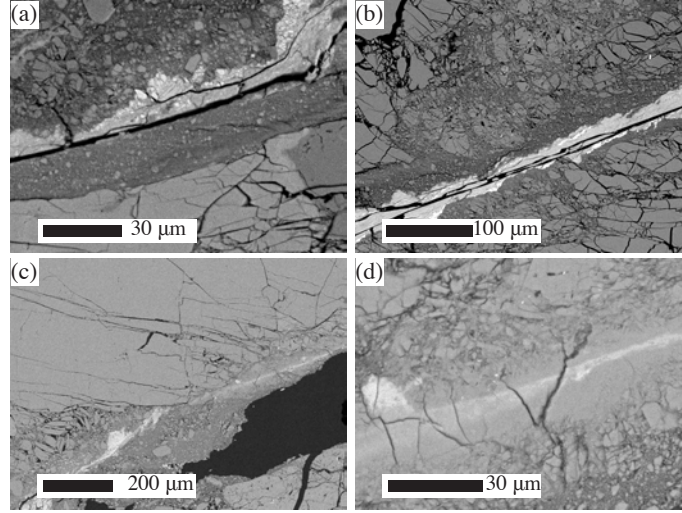


Figure 8: Fault zone structure in the sample tested at $P_c = 70$ MPa and $P_f = 30$ MPa. (a–d) SEM Backscattered electron images of the thin shear zones occurring within the fault gouge layer. In image (c), the large black region is an area where the gouge material was lost during sample preparation.

8c,d). These textures are very similar to those reported by *Hayward and Cox* (2017) in faulted sandstone, and could be interpreted as welded patches made of glass, potentially cooled from a frictional melt. More detailed analyses would be needed to confirm the potential melt origin of such textures, knowing that amorphous material can be produced without melting (e.g., *Yund et al.*, 1990; *Pec et al.*, 2012). In any case, such an extreme grain size reduction, compaction, and the presence of elongated flow structures indicate that strain was strongly localised along a set of internal shear zones after the main fault-forming rupture event.

Overall, microstructural investigations indicate that the dilation responsible for pore pressure fluctuations during rupture and slip was localised within the fault zone itself, as evidenced by the heavily cracked, porous gouge layer formed inside the fault, and the relatively narrow damage zone around it. The overall waviness of the fault most likely contributed significantly to slip-induced opening.

5 Discussion

5.1 Fluid pressure drop and localised dilatancy during rupture

The experimental data show a systematic drop in fluid pressure during the main rupture and each slip event, associated with localised dilatancy on the fault plane. These data provide direct evidence of the “seismic suction pump” model of *Sibson (1987)*. During rupture, the measurements of on-fault pore pressure show very rapid drops to near-zero values, while off-fault measurements are more gradual and do not reach zero. These results can be explained by localised dilatancy within the fault zone, which depressurises directly the fluid inside the fault, and induces a diffusive fluid flux that makes the pressure drop gradually propagate into off-fault regions.

The on-fault fluid pressure remained stable at near-zero values during a few minutes after rupture (Figures 2f, S8f). If a constant fluid compressibility was assumed, we would expect an immediate pore pressure recharge after the drop (similar to that observed immediately after stick-slip events, where the pore pressure drop was relatively modest, see Figure 4c). This discrepancy is resolved by considering that the pore fluid either degases or vaporises due to rapid isothermal decompression, producing an apparent increase in fluid compressibility, therefore stabilising the fluid pressure in the fault.

In the sample tested at $P_c = 70$ MPa and $P_f = 30$ MPa, the total pore volume change measured after complete post-failure reequilibration was 0.37 cm^3 , which corresponds to a porosity change of +5% in a 3 mm-wide fault zone. Under undrained, isothermal conditions, the fluid mass conservation leads to a pressure change expressed as

$$\Delta p = -\ln(\phi\rho(p)/\phi_0\rho_0)/C_{pp}, \quad (1)$$

where C_{pp} is the pore space compressibility, ϕ and ϕ_0 are the final and initial porosity, ρ_0 is the initial fluid density and $\rho(p)$ is the fluid density at pressure p . Neglecting the compressibility of the solid grains of the rock and using an initial porosity of $\phi_0 = 2\%$, an upper bound estimate for C_{pp} is $5 \times 10^{-9} \text{ Pa}^{-1}$ (estimated as the ratio of storage capacity and porosity, see Figures 1 and S5). Starting from 30 MPa and using pressure-dependent variations in fluid density (*Junglas, 2009*), the vaporisation pressure (≈ 3 kPa at room temperature) is reached after a porosity increase of only 0.3%. Even considering a pore space compressibility increased by a factor 10 to simulate the effect of damage (e.g., *Noda et al., 2009; Brantut and Mitchell, 2018*), the vaporisation pressure is reached after a porosity increase of around 3%. Therefore, the pore fluid could be at least partially vaporised due to the fault zone dilatancy during rupture. It is unclear how much dissolved gas was present in the pore fluid prior to rupture events, but degassing of dissolved air is expected to occur during decompression, which could also contribute significantly to increasing the apparent compressibility of the pore fluid and stabilising the pore pressure after rupture.

In the experiments, shear failure of initially intact (notched) rock samples produced spontaneously a non-planar fault geometry at centimetre scale (Figure 7a), which allowed us to capture multiple dilatancy mechanisms: initial coalescence of microcracks to form the through-going fault, granular packing variations within the gouge, microfracturing of wall rock (off-fault) and of cohesive lenses of material embedded in the gouge (Figure 7,b,c), and opening of dilational jogs. Taken together, these dilatant processes resulted in dramatic pore pressure drops during rupture. The non-planar geometry of natural faults, with the presence of local dilational jogs, has been considered as a key factor controlling fluid pressure variations and redistribution along faults (*Sibson, 1987, 1994*). The experimental data therefore provide direct evidence supporting the conclusions drawn from field observations that coseismic dilatancy can locally depressurise fluids and induce phase separation, mineral precipitation and gold deposition (e.g., *Sibson, 1987; Wilkinson and Johnston, 1996; Cox, 1999; Wilkinson, 2001; Weatherley and Henley, 2013; Peterson and Mavrogenes, 2014*).

5.2 Seismic signature of dilatancy during rupture

In the experiments, the signal observed in seismic wave speeds was quite complex (Figure 3): while some areas and orientations were severely impacted by the main rupture and a clear signal could be attributed to pore pressure recharge (see the second drop in P wave speed along paths A and B), such observations are not ubiquitous and depend on the details of the ray paths geometry. This complexity reflects the strong localisation of microcrack damage during rupture (*Aben et al., 2019*), which in turn impacts the localisation of dilatancy and pore pressure variations. Dilatant microcracking has two competing effects on wave velocities: (1) a direct effect, whereby microcracks tend to decrease elastic wave speeds (preferably in orientations perpendicular to crack faces, see for instance *Sayers and Kachanov (1995)*), and (2) an indirect effect, whereby dilation-induced drops in pore pressure tend to close existing or newly formed microcracks through an increase in effective mean stress. The direct effect is very strong and localised, leading to the first observed drop in P wave speed along paths A and B. The indirect effect is of second order, but leads to clear variations as evidenced by the second, more gradual decrease in wave speed observed in the experiment.

While a sufficient level of detail can be achieved in laboratory observations to provide a clear interpretation of the results, evidences for pore pressure drops would be challenging to detect seismologically in a systematic way in nature. Seismological data consistently indicate that wave speeds decrease around fault zones after earthquakes (e.g., *Schaff and Beroza, 2004; Li et al., 2006; Froment et al., 2014*), which has been attributed to damage generation or reactivation. However, such observations typically represent a spatial and temporal average of the changes within a volume surrounding the fault. The effect of a pore pressure drop on wave speeds is of second order, and is linked to the positive correlation between wave speeds and effective pressure in fractured media. The effect of pore pressure change on wave speeds is not only small in comparison to the direct

effect of microcrack damage, but is also strongly localised in space and transient in time. Therefore, wave speed monitoring would require a high spatio-temporal resolution together with a high precision to be interpreted unambiguously.

5.3 Coseismic dilatancy hardening and impact on weakening mechanisms

Dilatancy is shown here to be the dominant process driving pore pressure change during the early stages of slip along a fresh fault with realistic roughness. Dilatancy effectively resets the fluid pressure to lower values at the onset of seismic slip, and tends to counteract the thermal pressurisation process as slip proceeds (*Rice*, 2006). The experimental data provide unique constraints on the key parameters governing the effect of dilatancy on pore pressure variations.

Microstructural observations unambiguously indicate that the sample pore volume change was localised in the fault zone. Therefore, the evolution of net pore volume change as a function of slip (as measured by taking the difference between intensifier volume before and after slip) can be used to make elementary predictions of the expected pore pressure change during earthquakes. The pore volume change appears to be roughly a linear function of the accumulated slip (Figure 6a). The rate of pore volume change per increment of slip differs quite significantly (by a factor of around 2.5) between the two experiments, but remains of a similar order of magnitude. Such a variability likely reflects slight variations in fault geometry due to the spontaneous rupture process, as well as the use of a different combination of confining and nominal fluid pressure between the two tests. Regardless of such variations, a linear increase in fault opening with increasing slip can be explained by the rough fault profile, with overriding asperities generating net opening as slip proceeds. Observations are limited since only a few millimetres of slip could be imposed during the experiments, but it is unlikely that fault opening can keep increasing linearly as very large slip is accumulated. Fault wear rates decrease dramatically after the first few centimetres of slip (e.g., *Scholz*, 2019, Chap. 2). In addition, as the fault matures, fault wear (and the associated microcracking and dilatancy) is expected to reduce the roughness along strike and thicken the gouge zone (*Scholz*, 2019, Chap. 3). Therefore, extrapolation of the experimental dilatancy data to a wider range of slip distances requires a transition from large to small dilation rate beyond some critical slip distance.

A simple, natural quantitative description of the change in porosity during slip is therefore given by

$$\phi(\delta) = \phi_0 + (\phi_{\max} - \phi_0)(1 - e^{-\delta/\delta_D}), \quad (2)$$

where ϕ_0 is the initial porosity of the fault, ϕ_{\max} is the asymptotic porosity at large slip, δ is slip and δ_D is a characteristic slip displacement over which dilatancy occurs. A realistic value for the maximum porosity ϕ_{\max} is that of a random packing of spheres, which is around 35%. Considering a fault width of 3 mm, the experimental measurements of fluid volume change after each slip

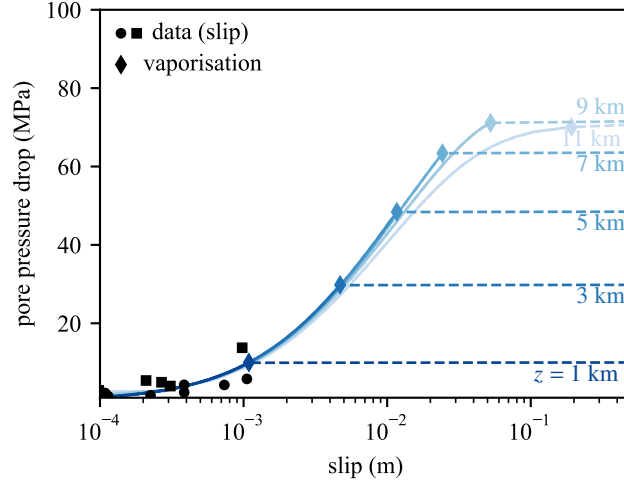


Figure 9: Isothermal, undrained pore pressure drop as a function of slip for a range of depths. Black circles and squares show laboratory data obtained during slip in the tests conducted at $(P_c, P_f) = (70, 30)$ and $(P_c, P_f) = (60, 20)$, respectively. Diamonds indicate points where fluid vaporisation occurs. An initial porosity of 2% was used. At each depth, the initial pore pressure is assumed hydrostatic, and the initial temperature is computed using a 40°C km^{-1} geotherm.

event (Figure 6a) can be converted into fault zone porosity changes ranging from +0.42% to +1.12% at around 1 mm slip. Values of $\delta_D = 0.08$ and 0.03 m, respectively, are in agreement with these observations. The measurements of pore pressure drop associated with each slip event (Figure 6b) provide a constraint on the pore space compressibility $C_{pp} \approx 2 - 4 \times 10^{-8} \text{ Pa}^{-1}$.

Combining the porosity model (Equation 2) with the governing equation for fluid pressure change (Equation 1), the isothermal, undrained pore pressure drop is computed for a range of slip distances and depths across the seismogenic crust (Figure 9, where average parameter values of $\delta_D = 0.05 \text{ m}$, $\phi_0 = 2\%$, $\phi_{\max} = 35\%$ and $C_{pp} = 3 \times 10^{-8} \text{ Pa}^{-1}$ have been assumed). Under these conditions, total fluid pressure drops (i.e., down to degassing or vapor pressure) are predicted at the early stages of slip (typically less than 1 cm) throughout the upper 9 km of the crust. Considering the variability and limited accuracy of laboratory-derived parameters, and the simplicity of the proposed dilatancy model, the numerical results given in Figure 9 should be viewed only as order-of-magnitude estimates. Significant deviations from these estimates are expected depending on the degree of fault core consolidation or healing (as observed experimentally, intact rocks experience dramatically more dilation than preexisting faults), as well as from local variations in fault geometry (e.g., more dilation expected in dilational jogs). While a systematic experimental characterisation of

these effects is currently missing, the present data indicate that on-fault dilation contributes significantly to coseismic pore pressure changes, which potentially impacts dynamic weakening mechanisms such as thermal pressurisation.

Pore pressure drops due to dilatancy are unlikely to be overcome or even balanced by shear heating effects: the thermal pressurisation factor, which relates the temperature rise to the pore pressure rise, is expected to be very small in freshly faulted rocks (as in our experiments), because the pore space compressibility is much larger than in intact rocks. Using a representative value of $C_{pp} = 3 \times 10^{-8} \text{ Pa}^{-1}$, a realistic estimate for the thermal pressurisation factor is 0.03 MPa K^{-1} (Brantut and Platt, 2017), so that the slip weakening distance associated with thermal pressurisation is of the order of 0.12 m, which is significantly larger than the slip required to induce complete pore pressure drops in the upper part of the crust (Figure 9).

The slip-dependent dilatancy model proposed here (Equation 2) based on friction tests along freshly fractured rocks differs from the rate-and-state dependent model of Segall and Rice (1995), which is based on quasistatic synthetic gouge experiments from Marone *et al.* (1990). While the Segall and Rice (1995) model has been widely used in the context of earthquake nucleation and slow slip (e.g., Segall *et al.*, 2010), including couplings with thermal pressurisation (Segall and Rice, 2006; Segall and Bradley, 2012), it has been unclear whether it could be used to simulate rapid seismic slip. In that model, fault gouge porosity variations are linked to slip rate in the form (Segall and Rice, 1995)

$$\frac{d\phi}{dt} = -\frac{v}{d_c}(\phi - \phi_{ss}), \quad (3)$$

$$\phi_{ss} = \phi_0 + \epsilon \ln(v/v^*), \quad (4)$$

where v is the slip rate, v^* is a reference (slow) slip rate, d_c is a slip-weakening distance (of the order of $10 \text{ } \mu\text{m}$), and ϵ is a dilation parameter of the order of 10^{-4} as per Marone *et al.* (1990). Following a step increase in slip rate from v^* to a larger value V , for instance to simulate a sudden slip episode such as stick-slip, the porosity evolution is of the form

$$\phi(\delta) = \phi_0 + (\epsilon \ln(V/v^*))(1 - e^{-\delta/d_c}), \quad (5)$$

which is similar to our simple approximation (equation 2). However, the order of magnitude of the parameters is vastly different. The critical slip distance d_c is approximately 1000 times smaller than our inferred δ_D , and for an increase in slip rate from, say, $1 \text{ } \mu\text{m/s}$ to 1 m/s , the maximum porosity increase would only be of +0.14%, far less than reported in our experiments on freshly fractured rock. The discrepancy between the two datasets and models can be explained by the rough fault geometry of the fresh faults, which appears to dominate their dilatant response.

While further analysis is required to investigate fully how dilatancy and thermal pressurisation are coupled during seismic slip, the present laboratory experiments clearly demonstrate the possibility that rupture induces pore pressure drops in crystalline rocks. These results highlight that the occurrence of

dilatancy is likely the major difference between faults hosted in intact or healed crystalline rocks and mature faults containing fine-grained gouge and clay minerals. In the former, pseudotachylytes are not uncommon (*Sibson and Toy, 2006*) and at depths of 10 to 20 km in the crust, where temperature is elevated and fluid-rock interactions are relatively fast, post-seismic fault sealing should rapidly cement fault rocks, so that fault reactivation during subsequent earthquakes requires re-fracturing of the fault core. In regions where cementation and fault sealing are fast compared to interseismic periods, large dilatancy effects are expected during earthquake propagation. In mature faults and at shallower depths, pseudotachylytes are rare and thin slip zones with clay-bearing gouges might allow very little overconsolidation and negligible dilatancy. There, thermal pressurisation might be a very effective mechanism (*Rice, 2006*). The role of dilatancy appears to be a key test to determine the dominant weakening mechanism in earthquakes: while seismological data are consistent with thermal pressurisation across wide range of magnitudes (*Viesca and Garagash, 2015*), other mechanisms with similar seimological signatures are likely operating (e.g., flash heating or melting, *Nielsen et al., 2008*; *Di Toro et al., 2011*; *Violay et al., 2015*; *Brantut and Viesca, 2017*). Our laboratory measurements of pore pressure drop on newly formed faults with realistic geometries and internal structures constitute a first clear observation that thermal pressurisation might be less ubiquitous than previously thought.

6 Conclusions

Direct pore pressure measurements show that during experimental shear faulting of granite, localised fault dilatancy is large enough to decompress the saturating pore fluid from several tens of megapascals down to vapor pressure. Slip on the newly formed faults is also accompanied with net dilation, and, for high enough slip rates, pore pressure drops. The roughness of the spontaneously formed faults plays a key role in producing such strong dilatant effects, which are orders of magnitude stronger than predicted by models based on gouge deformation in planar faults. The laboratory observations presented here provide a quantitative, direct evidence of the “seismic suction pump” concept developed by *Sibson (1987)*. The large fault dilatancy occurring during faulting of intact rocks and slip on fresh faults indicate that dynamic weakening by thermal pressurisation is unlikely to be dominant in those materials, and that other weakening mechanisms must play a role.

Acknowledgments

Neil Hughes provided technical support for the manufacture of the fluid pressure transducers. Discussions with Frans Aben, Dmitry Garagash, Nadia Lapusta, Philip Meredith and Alexandre Schubnel contributed to shape this project. Comments from two anonymous reviewers on a previous draft helped tremen-

dously with the discussion of the results. Financial support from the UK Natural Environment Research Council (grants NE/K009656/1, NE/M016471/1 and NE/S000852/1) and from the European Research Council under the European Union’s Horizon 2020 research and innovation programme (project RockDEaF, grant agreement #804685) is acknowledged.

References

- Aben, F. M., N. Brantut, T. M. Mitchell, and E. C. David, Rupture energetics in crustal rock from laboratory-scale seismic tomography. geophysical research letters, *Geophys. Res. Lett.*, *46*, 7337–7344, doi:10.1029/2019GL083040, 2019.
- Brace, W. F., and R. J. Martin, A test of the law of effective stress for crystalline rocks of low porosity, *Int. J. Rock Mech. Min. Sci.*, *5*, 415–426, 1968.
- Brace, W. F., B. W. Paulding Jr., and C. Scholz, Dilatancy in the fracture of crystalline rocks, *J. Geophys. Res.*, *71*(16), 3939–3953, 1966.
- Brantut, N., and T. M. Mitchell, Assessing the efficiency of thermal pressurisation using natural pseudotachylyte-bearing rocks, *Geophys. Res. Lett.*, *45*, 9533–9541, doi:10.1029/2018GL078649, 2018.
- Brantut, N., and J. D. Platt, Dynamic weakening and the depth dependence of earthquake faulting, in *Fault Zone Dynamic Processes: Evolution of Fault Properties During Seismic Rupture*, *Geophys. Monogr. Ser.*, vol. 227, edited by M. Y. Thomas, T. M. Mitchell, and H. S. Bhat, pp. 171–194, American Geophysical Union, Washington, DC, 2017.
- Brantut, N., and R. C. Viesca, The fracture energy of ruptures driven by flash heating, *Geophys. Res. Lett.*, *44*, 6718–6725, doi:10.1002/2017GL074110, 2017.
- Cox, S. F., Deformational controls on the dynamics of fluid flow in mesothermal gold systems, in *Fractures, Fluid Flow and Mineralization, Special Publications*, vol. 155, edited by K. J. W. McCaffrey, L. Lonergan, and J. J. Wilkinson, pp. 123–140, Geological Society, London, 1999.
- Di Toro, G., R. Han, T. Hirose, N. De Paola, S. Nielsen, K. Mizoguchi, F. Ferri, M. Cocco, and T. Shimamoto, Fault lubrication during earthquakes, *Nature*, *471*, 494–498, 2011.
- Eccles, D., P. R. Sammonds, and O. C. Clint, Laboratory studies of electrical potential during rock fracture, *Int. J. Rock Mech. Min. Sci.*, *42*(7-8), 933–949, 2005.
- Ferri, F., G. Di Toro, T. Hirose, and T. Shimamoto, Evidence of thermal pressurization in high-velocity friction experiments on smectite-rich gouges, *Terra Nova*, *22*, 347–353, 2010.

- Froment, B., J. J. McGuire, R. D. van der Hilst, P. Gouédard, E. C. Roland, H. Zhang, and J. A. Collins, Imaging along-strike variations in mechanical properties of the Gofar transform fault, East Pacific Rise, *J. Geophys. Res.*, *119*(9), 7175–7194, doi:10.1002/2014JB011270, 2014.
- Hayward, K. S., and S. F. Cox, Melt welding and its role in fault reactivation and localization of fracture damage in seismically active faults, *J. Geophys. Res.*, *122*, 9689–9713, 2017.
- Junglas, P., WATER95—A MATLAB®implementation of the IAPWS-95 standard for use in thermodynamics lectures, *Int. J. Engng. Ed.*, *25*(1), 3–18, 2009.
- Li, Y.-G., P. Chen, E. S. Cochran, J. E. Vidale, and T. Burdette, Seismic evidence for rock damage and healing on the San Andreas fault associated with the 2004 *m* 6.0 Parkfield earthquake, *Bull. Seism. Soc. Am.*, *96*(4B), S349–S363, 2006.
- Marone, C., C. B. Raleigh, and C. H. Scholz, Frictional behavior and constitutive modeling of simulated fault gouge, *J. Geophys. Res.*, *95*(B5), 7007–7025, 1990.
- Martin, R. J., Pore pressure stabilization of failure in Westerly granite, *Geophys. Res. Lett.*, *7*(5), 404–406, 1980.
- Morrow, C. A., and J. D. Byerlee, Experimental studies of compaction and dilatancy during frictional sliding on faults containing gouge, *J. Struct. Geol.*, *11*(7), 815–825, 1989.
- Nielsen, S., G. Di Toro, T. Hirose, and T. Shimamoto, Frictional melt and seismic slip, *J. Geophys. Res.*, *113*, B01308, doi:10.1029/2007JB005122, 2008.
- Noda, H., E. M. Dunham, and J. R. Rice, Earthquake ruptures with thermal weakening and the operation of major faults at low overall stress levels, *J. Geophys. Res.*, *114*, B07302, doi:10.1029/2008JB006143, 2009.
- Parry, W. T., Fault-fluid compositions from fluid inclusion observations and solubilities of fracture-sealing minerals, *Tectonophysics*, *290*, 1–26, 1998.
- Paterson, M. S., and T. F. Wong, *Experimental Rock Deformation – The Brittle Field*, 2nd ed., Springer-Verlag, Berlin Heidelberg, 2005.
- Pec, M., H. Stünitz, R. Heilbronner, M. Drury, and C. de Capitani, Origin of pseudotachylites in slow creep experiments, *Earth Planet. Sci. Lett.*, *355–356*, 299–310, 2012.
- Peterson, E. C., and J. A. Mavrogenes, Linking high-grade gold mineralization to earthquake-induced fault-valve processes in the Porgera gold deposit, Papua New Guinea, *Geology*, *42*(5), 383–386, 2014.

- Rempel, A., and J. R. Rice, Thermal pressurization and onset of melting in fault zones, *J. Geophys. Res.*, *111*, B09314, doi:10.1029/2005JB004006, 2006.
- Rice, J. R., On the stability of dilatant hardening for saturated rock masses, *J. Geophys. Res.*, *80*(11), 1531–1536, 1975.
- Rice, J. R., Heating and weakening of faults during earthquake slip, *J. Geophys. Res.*, *111*, B05311, doi:10.1029/2005JB004006, 2006.
- Rudnicki, J. W., and C.-H. Chen, Stabilization of rapid frictional slip on a weakening fault by dilatant hardening, *J. Geophys. Res.*, *93*, 4745–4757, 1988.
- Samuelson, J., D. Elsworth, and C. Marone, Shear-induced dilatancy of fluid-saturated faults: Experiment and theory, *J. Geophys. Res.*, *114*, B12404, doi:10.1029/2008JB006273, 2009.
- Sayers, C., and M. Kachanov, Microcrack-induced elastic wave anisotropy of brittle rocks, *J. Geophys. Res.*, *100*(B3), 4149–4156, 1995.
- Schaff, D. P., and G. C. Beroza, Coseismic and postseismic velocity changes measured by repeating earthquakes, *J. Geophys. Res.*, *109*, B10302, doi:10.1029/2004JB003011, 2004.
- Scholz, C. H., *The mechanics of earthquakes and faulting*, Cambridge University Press, New York, NY, 2019.
- Segall, P., and A. M. Bradley, The role of thermal pressurization and dilatancy in controlling the rate of fault slip, *J. Appl. Mech.*, *79*, 031,013, 2012.
- Segall, P., and J. R. Rice, Dilatancy, compaction, and slip instability of a fluid-infiltrated fault, *J. Geophys. Res.*, *100*(B11), 22,155–22,171, 1995.
- Segall, P., and J. R. Rice, Does shear heating of pore fluid contribute to earthquake nucleation?, *J. Geophys. Res.*, *111*, B09316, doi:10.1029/2005JB004129, 2006.
- Segall, P., A. M. Rubin, A. M. Bradley, and J. R. Rice, Dilatant strengthening as a mechanism for slow slip events, *J. Geophys. Res.*, *115*, B12305, doi:10.1029/2010JB007449, 2010.
- Sibson, R. H., Earthquake rupturing as a mineralizing agent in hydrothermal systems, *Geology*, *15*, 701–704, 1987.
- Sibson, R. H., Crustal stress, faulting and fluid flow, in *Geofluids: Origin, Migration and Evolution of Fluids in Sedimentary Basins, Special Publications*, vol. 78, edited by E. J. Parnell, pp. 69–84, Geological Society, London, 1994.
- Sibson, R. H., and V. G. Toy, The habitat of fault-generated pseudotachylyte: presence vs. absence of friction melt, in *Earthquakes: radiated energy and the physics of faulting, Geophys. Monogr. Ser.*, vol. 170, edited by R. Abercrombie, A. McGarr, G. Di Toro, and H. Kanamori, pp. 153–166, American Geophysical Union, Washington, DC, 2006.

- Sibson, R. H., J. M. Moore, and A. H. Rankin, Seismic pumping – a hydrothermal fluid transport mechanism, *J. Geol. Soc. Lond.*, *131*, 653–659, 1975.
- Viesca, R. C., and D. I. Garagash, Ubiquitous weakening of faults due to thermal pressurization, *Nat. Geosci.*, doi:10.1038/ngeo2554, 2015.
- Violay, M., G. Di Toro, S. Nielsen, E. Spagnuolo, and J. P. Burg, Thermo-mechanical pressurization of experimental faults in cohesive rocks during seismic slip, *Earth Planet. Sci. Lett.*, *429*, 1–10, 2015.
- Wang, X.-Q., A. Schubnel, J. Fortin, Y. Guéguen, and H.-Q. Ge, Physical properties and brittle strength of thermally cracked granite under confinement, *J. Geophys. Res.*, *118*, 6099–6112, doi:10.1002/2013JB010340, 2013.
- Weatherley, D. K., and R. W. Henley, Flash vaporization during earthquakes evidenced by gold deposits, *Nat. Geosci.*, *6*, 294–298, 2013.
- Wilkinson, J. J., Fluid inclusions in hydrothermal ore deposits, *Lithos*, *55*, 229–272, 2001.
- Wilkinson, J. J., and J. D. Johnston, Pressure fluctuations, phase separation, and gold precipitation during seismic fracture propagation, *Geology*, *24*(5), 395–398, 1996.
- Yund, R. A., M. L. Blanpied, T. E. Tullis, and J. D. Weeks, Amorphous material in high strain experimental fault gouges, *J. Geophys. Res.*, *95*(B10), 15,589–15,602, 1990.
- Zoback, M. D., and J. D. Byerlee, The effect of microcrack dilatancy on the permeability of Westerly granite, *J. Geophys. Res.*, *80*(5), 752–755, 1975.